Check for updates

AGU ADVANCING EARTH AND SPACE SCIENCES

Geophysical Research Letters®

RESEARCH LETTER
10.1029/2025GL120284

Superposition of Doppler-Shifting Magnetopause Kelvin-Helmholtz Modes Through Dynamic Mode Decomposition of a Global MHD Simulation

H. M. Kelly[1,2], **M. O. Archer**[1], **J. P. Eastwood**[1], **M. Heyns**[1,3], **J. W. B. Eggington**[1,4], and **J. P. Chittenden**[1]

[1]Space, Plasma & Climate Physics, Department of Physics, Imperial College London, London, UK, [2]Now at Met Office, Exeter, UK, [3]Now at Trillium Technologies, London, UK, [4]Now at EDF R&D UK Centre, London, UK

Key Points:

- Using a spatio-temporal dimensionality-reduction algorithm, we assess Kelvin-Helmholtz generation and evolution in a global magnetohydrodynamic simulation
- Locally generated waves persist downstream continually growing, leading to a spatially varying superposition that affects the dominant mode
- Each mode has fixed frequency but an increasing wavelength downtail due to a Doppler shift by the accelerating advective magnetosheath flow

Supporting Information:

Supporting Information may be found in the online version of this article.

Correspondence to:

M. O. Archer,
m.archer10@imperial.ac.uk

Citation:

Kelly, H. M., Archer, M. O., Eastwood, J. P., Heyns, M., Eggington, J. W. B., & Chittenden, J. P. (2026). Superposition of Doppler-shifting magnetopause Kelvin-Helmholtz modes through dynamic mode decomposition of a global MHD simulation. *Geophysical Research Letters*, *53*, e2025GL120284. https://doi.org/10.1029/2025GL120284

Received 27 OCT 2025
Accepted 21 APR 2026

Author Contributions:

Conceptualization: M. O. Archer
Data curation: H. M. Kelly
Formal analysis: H. M. Kelly
Funding acquisition: M. O. Archer
Investigation: H. M. Kelly
Methodology: H. M. Kelly
Project administration: M. O. Archer
Software: M. Heyns, J. W. B. Eggington, J. P. Chittenden
Supervision: M. O. Archer, J. P. Eastwood
Validation: H. M. Kelly, M. Heyns, J. W. B. Eggington
Visualization: H. M. Kelly, M. O. Archer

Abstract

The Kelvin-Helmholtz instability (KHI) mediates the viscous-like solar-terrestrial interaction by generating magnetopause surface waves that quickly become non-linear. Basic theory predicts the locally most-unstable linear wave dominates. However, Kelvin-Helmholtz is a broad, convective instability that also amplifies waves originating upstream. We address this conundrum by applying dynamic mode decomposition to a Gorgon global magnetohydrodynamic simulation of the KHI. While distinct modes quickly grow at points along the magnetopause, signaling local generation, their energy continues to slowly grow downtail. Thus, a superposition is present along the magnetopause, where the dominant mode is not always the locally fastest-growing. Each mode's wavelength elongates downtail, correlating with the boundary layer flow speed due to the accelerating advective flow around the magnetosphere Doppler shifting the fixed-frequency waves. This may explain why longer wavelengths are observed in the tail than theory predicts and motivates further exploration of tangential inhomogeneities in basic Kelvin-Helmholtz theory.

Plain Language Summary

The solar wind flowing around the obstacle of Earth's magnetosphere generates waves on its boundary, akin to surface waves growing on water from the wind blowing above it. These Kelvin-Helmholtz waves play a key role in allowing solar wind plasma and energy to penetrate our magnetic shield. Determining when and where this should occur and which wave modes grow has remained challenging. This is because the underlying theory has concentrated on local wave growth, whereas these waves travel along the boundary into new regions with different properties, which in turn should affect the waves. Two possible paradigms exist, waves are either: (a) locally generated, being those predicted by the simple theory; or (b) originate further upstream, having traveled and grown along the way. We apply a machine learning technique that efficiently extracts distinct wave modes from a simulation of the entire magnetosphere. This shows Kelvin-Helmholtz waves do grow quickly out of some points on the boundary, though their energy persists as they travel down the tail, slowly growing in both amplitude and spatial extent in the process. Both effects play a role in which waves are dominant at any point.

1. Introduction

The Kelvin-Helmholtz instability (KHI) from velocity shear across the magnetopause drives tailward-traveling surface wave growth (Archer et al., 2024; Chandrasekhar, 1961) and evolution into non-linear rolled-up vortices (Hasegawa et al., 2004; Miura, 1982). It is key to the viscous-like solar-terrestrial interaction (Axford & Hines, 1961) mediating mass, momentum, and energy transport into geospace (Faganello & Califano, 2017; Johnson et al., 2014; Kivelson & Chen, 1995; Masson & Nykyri, 2018; Rice et al., 2024).

Linear KH-theory has analytic solutions only for tangential discontinuities separating homogeneous, incompressible fluids (Chandrasekhar, 1961; Sen, 1963), with the magnetopause being KH-unstable if shear stress overcomes magnetic tension, that is,

$$\gamma^2 = \frac{\rho_{\mathrm{msp}}\rho_{\mathrm{msh}}}{(\rho_{\mathrm{msp}}+\rho_{\mathrm{msh}})^2}[\mathbf{k}\cdot(\mathbf{v}_{\mathrm{msh}}-\mathbf{v}_{\mathrm{msp}})]^2 - \frac{1}{\mu_0(\rho_{\mathrm{msp}}+\rho_{\mathrm{msh}})}\left[(\mathbf{k}\cdot\mathbf{B}_{\mathrm{msp}})^2+(\mathbf{k}\cdot\mathbf{B}_{\mathrm{msh}})^2\right] > 0 \quad (1)$$

for growth rate γ, wave vector $\mathbf{k}$, velocities $\mathbf{v}$, mass densities ρ, and magnetic fields $\mathbf{B}$, where subscripts "msp" and "msh" denote the magnetosphere and magnetosheath, respectively. Notably, the growth rate is proportional to

Writing – original draft: M. O. Archer
Writing – review & editing: H. M. Kelly, J. P. Eastwood, M. Heyns, J. W. B. Eggington

wavenumber. This criterion, despite its limitations, is still widely used (Grimmich et al., 2025; Rice et al., 2022). Southwood (1968) showed low-/mid-latitude KH-modes are most unstable when $\mathbf{k}$ is perpendicular to $\mathbf{B}_{\mathrm{msp}}$. The instability thus maximizes when the interplanetary magnetic field (IMF) is either northward or southward (southward IMF also favors large-scale magnetic reconnection, Trattner et al., 2021), consistent with observational statistics (Kavosi & Raeder, 2015; Kavosi et al., 2023). However, the full KH problem must be solved numerically (Pu & Kivelson, 1983).

Introducing boundary thickness, width d, yields distinct KH-modes forming at different interfaces/transitions (Lee et al., 1981) whose basic wave properties (frequency, wavelength, and phase speed) and growth rates may differ. Whether these modes are independent or coupled depends on the wave amplitude relative to d (Kivelson & Pu, 1984). When compressibility is also included, numerical results predict the boundary is KH-unstable for $0 \leq kd < 2$ (Miura & Pritchett, 1982; Walker, 1981) (subject to Equation 1 holding also). This introduces a fastest-growing KH-mode with $kd \sim 0.5$–1, verified in local simulations (Briard et al., 2024). Its frequency follows from combining the (frame-independent) wavelength and phase/vortex velocity, typically between the center-of-mass and average flow velocities (Hasegawa et al., 2009; Palermo et al., 2011). Observed magnetopause KH-waves are often assumed to be the locally fastest-growing linear KH-mode (Hasegawa et al., 2004; Lin et al., 2014). However, several case studies (Belmont & Chateur, 1989; Hastie et al., 2009) and statistics (Zhou et al., 2022) show longer wavelengths than expected, particularly in the far tail.

The KHI is a broad instability—in its linear stages it amplifies existing seed fluctuations across $0 \leq kd < 2$. Local simulations show that with turbulent velocity/magnetic field fluctuations the dominant KH-mode can have a longer wavelength than linear theory predicts since the instability amplifies the pre-existing perturbations (Nakamura et al., 2020; Nykyri et al., 2017). This challenges the assumption that the locally fastest-growing mode always dominates.

A purely local treatment of the KHI is inadequate. As a convective instability (Mills et al., 2000; Wu, 1986), KH-modes that grow under local plasma conditions are advected downtail into regions with markedly different plasma, magnetic fields, and boundary thicknesses (Haaland et al., 2019). These change not only the local KHI but affect the evolution of modes borne upstream. Therefore, it is unclear whether magnetopause waves at any given location have been locally generated or originated upstream and have been amplified. Currently only global (mostly magnetohydrodynamic [MHD]) simulations that reproduce the KHI in a representative magnetospheric system (Claudepierre et al., 2008; Collado-Vega et al., 2007; Slinker et al., 2003) can address this conundrum.

While simulations with similar northward IMF conditions generally find inner and outer mode KH-waves initially match the most-unstable linear mode from theory (Guo et al., 2010; Merkin et al., 2013; Michael et al., 2021), differences are reported in their evolution. Merkin et al. (2013) show under steady driving the locally fastest-growing mode dominates at all local times, though the spectrum is not monochromatic as each frequency decays slowly downstream. In contrast, Guo et al. (2010) find a single frequency along the magnetopause, set by the generation period of dayside vortices. Archer et al. (2021) report impulsively excited dayside magnetopause surface eigenmodes seed surface waves which the KHI amplifies, overriding intrinsic KH-frequencies. These differing results yield conflicting explanations for local-time variations in wavelengths.

To address the open question of how dominant KH-modes are generated and evolve globally, we employ a machine learning dimensionality-reduction technique for spatio-temporal data—dynamic mode decomposition (DMD)—to a Gorgon global MHD simulation of the KHI under northward IMF.

2. Simulation

The Gorgon MHD simulation code, originally developed for laboratory plasmas (Chittenden et al., 2004; Ciardi et al., 2007), was later adapted for Earth's magnetosphere (Desai et al., 2021; Eggington et al., 2018, 2020, 2022; Mejnertsen et al., 2018, 2021). It solves the resistive MHD equations on an Eulerian staggered Yee (1966) grid using the (Weyl/temporal gauge) magnetic vector potential and a split dipole (Tanaka, 1994) to preserve $\nabla \cdot \mathbf{B} = 0$. Here we use a uniform Cartesian grid of 0.25 $\mathrm{R_E}$ resolution spanning $x \in [-30, 90]$ $\mathrm{R_E}$ (pointing antisunward) and $y, z \in [-40, 40]$ $\mathrm{R_E}$ (the latter along the dipole), with an inner boundary at 4 $\mathrm{R_E}$ coupled to an ionosphere.

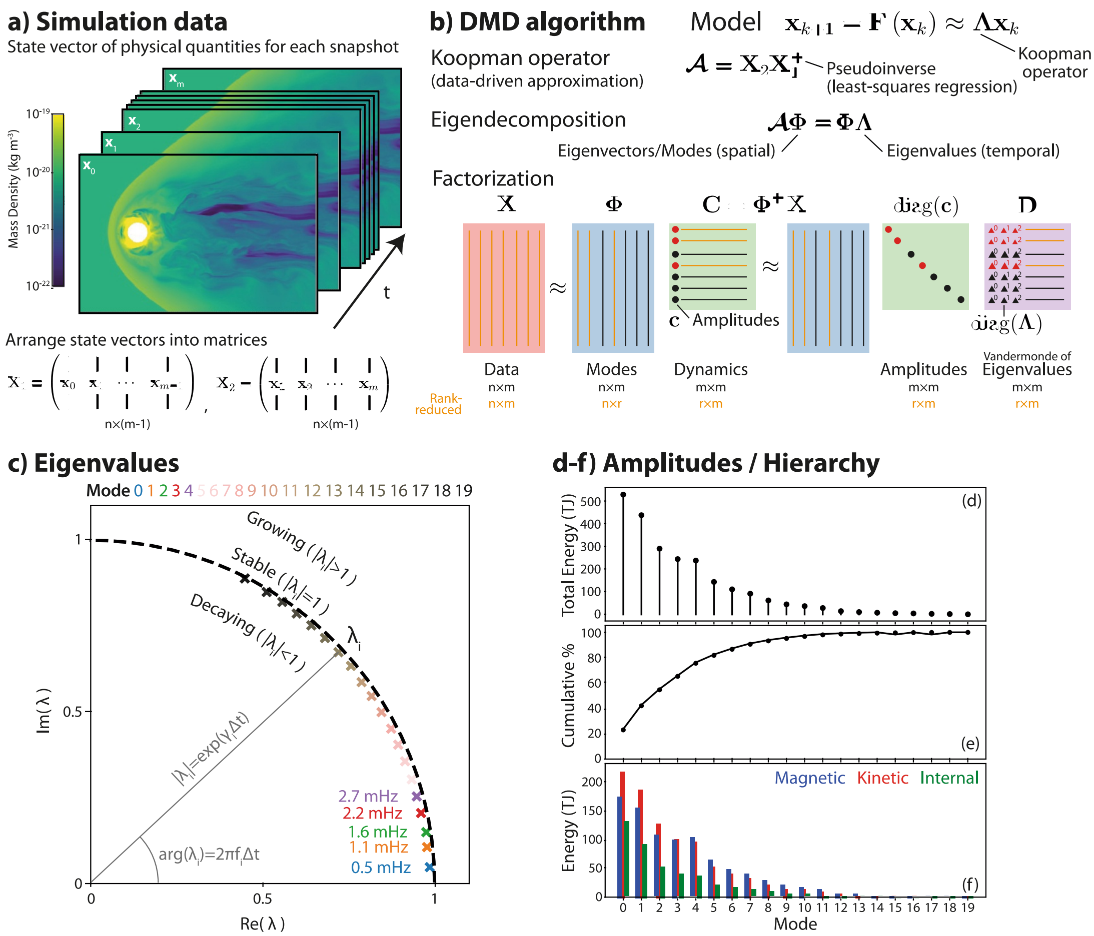

Figure 1. Overview of dynamic mode decomposition (DMD) applied to Gorgon simulation. (a) Simulation snapshots of mass density. (b) Outline of DMD algorithm. (c) Argand diagram of mode eigenvalues. (d–f) Mode hierarchy showing (d) total energy, (e) cumulative fraction, and (f) energy partition by mode number.

Solar wind plasma conditions were set to typical values, with speed 400 km s^{-1} and density 5 cm^{-3}. The magnetosphere was initialized under 2 h southward IMF $\mathbf{B} = (0, 0, -5)^T$ nT, followed by 2 h northward $\mathbf{B} = (0, 0, 5)^T$ nT—the most KH-unstable—reaching a quasi-steady state. Data was subsequently collected every 15 s for 27.5 min (110 snapshots). Further details are in Table S1 in Supporting Information S1.

The equatorial mass density (Figure 1a, Movie S1) shows clear non-linear waves along the magnetopause flanks characteristic of KHI (Claudepierre et al., 2008; Guo et al., 2010; Merkin et al., 2013). The analysis period spans approximately four wave periods of the clearest vortices. Using Equation 1, we confirmed the equatorial boundary is KH-unstable at a representative location. The high-resolution staggered grid produces turbulent dawn–dusk asymmetric magnetotail dynamics, for example, a transient fast return flow on the dawn (positive y) side (see Movie S1) which enhances this flank's velocity shear.

We wish to analyze the most significant, periodic behavior across the simulation. To do this efficiently, we introduce DMD.

3. Dynamic Mode Decomposition

Spatio-temporal data is often analyzed using linear Fourier methods, which neither reduce data volume nor represent time-varying oscillations compactly because of the Gabor uncertainty principle. DMD is a dimensionality-reduction machine learning algorithm that computes a set of modes, each with constant (continuously valued) data-driven oscillation frequencies and growth/decay rates (Schmid, 2010, 2022). It assumes the nonlinear system dynamics consists of coherent spatio-temporal structures that are locally linear and quasi-stationary

$$\mathbf{x}_{k+1} \approx \boldsymbol{\mathcal{A}}\mathbf{x}_k \tag{2}$$

where $\mathbf{x}_k$ is the system state vector at timestep k and $\boldsymbol{\mathcal{A}}$ approximates the Koopman (1931) operator, determined via least-squares regression. DMD performs eigen-decomposition of $\boldsymbol{\mathcal{A}}$, factorizing the original data (arranged into matrix $\mathbf{X}$ of snapshots $\mathbf{x}_k$) into the product of:

- Spatial information—normalized eigenvectors/modes $\boldsymbol{\phi}_i$
- Fluctuation magnitudes—diagonal matrix of global amplitudes c_i
- Temporal evolution—eigenvalues λ_i arranged in a Vandermonde matrix $\mathbf{D}$

as depicted in Figure 1b. This enables efficient spectral analysis, data reconstruction, and future state prediction from relatively sparse/reduced data in physically meaningful ways, unlike other dimensionality-reduction methods that lack intrinsic temporal behavior. All DMD outputs are complex-valued, which for real data necessitates modes exist in conjugate pairs. Further information is given in Text S1 in Supporting Information S1.

DMD was originally developed to analyze velocity fields in hydrodynamic simulations (Schmid, 2010), for example, nonlinear vortex shedding in wake flows. It has been applied in space physics to sunspot (Albidah et al., 2020) and ionospheric total electron content (Landa & Reuveni, 2023) observations, and for forecasting ionospheric/thermospheric densities (Alford-Lago et al., 2023; Mehta et al., 2018). These studies use a single physical quantity, but MHD dynamics depend on both the plasma and magnetic field. Standard machine learning normalizations (min-max, z-score; Hastie et al., 2009) are ad hoc, lack physical basis, and may artificially inflate/reduce physical importance between quantities. Since DMD involves minimizing variances, we scale MHD variables so their squared amplitudes are physically comparable. Guided by the energy density of MHD waves (Walker, 2005)

$$\mathcal{E} = \frac{1}{4}\rho_0 \delta\mathbf{v}\cdot\delta\mathbf{v}^* + \frac{\delta\mathbf{B}\cdot\delta\mathbf{B}^*}{4\mu_0} + \frac{\delta p \delta p^*}{4\rho_0 c_S^2} \tag{3}$$

where fluctuations denoted by δ's are complex phasors, subscript 0's denote time-averages over the entire analysis period, and c_S is the sound speed; we normalize (denoted by bars) the cell-centered velocity, magnetic field, and pressure fluctuations as

$$\delta\bar{\mathbf{v}} = \frac{1}{2}\sqrt{\rho_0}\delta\mathbf{v} \tag{4}$$

$$\delta\bar{\mathbf{B}} = \frac{1}{2\sqrt{\mu_0}}\delta\mathbf{B} \tag{5}$$

$$\delta\bar{p} = \frac{1}{2\sqrt{\gamma p_0}}\delta p \tag{6}$$

which have units of root energy density. The state vectors for each snapshot are then

$$\mathbf{x} = \left(\{\delta\bar{v}_x\},\{\delta\bar{v}_y\},\{\delta\bar{v}_z\},\{\delta\bar{B}_x\},\{\delta\bar{B}_y\},\{\delta\bar{B}_z\},\{\delta\bar{p}\}\right)^T \tag{7}$$

where braces represent the set of values across space.

Here we use the Singular Value Decomposition approach to DMD, which first reduces dimensionality via a discrete proper orthogonal decomposition (POD). We truncate the POD rank to 40 (slightly below the recommended maximum of 55, Rot et al., 2022), yielding 20 positive-frequency modes (negative-frequency conjugate modes are discarded). The length of analysis period used is appropriate for DMD since several cycles of pertinent wave dynamics are captured. The local-linearity, quasi-stationary assumption was checked through the determinant of $\boldsymbol{\mathcal{M}} = \ln(\boldsymbol{\mathcal{A}})/\Delta t$, which was $\sim 10^{-7}\times$ the Hadamard inequality upper-bound. The fractional residual was 0.378, meaning DMD captures most of the simulation dynamics; the remainder likely reflecting non-stationary behavior. See Text S1 in Supporting Information S1 for further discussion of these points.

4. Results

The KHI depends on local shear layer properties (thickness and plasma conditions). Since these are sensitive to simulation resolution and numerics (Archer et al., 2024), absolute wave properties (e.g., growth rates, wavelengths) vary between different simulations and reality (see Text S2 in Supporting Information S1 for discussion), though are consistent with KH-theory applied to their respective shear layers. We therefore focus here on the physics behind relative variations and relationships in wave properties within this single simulation.

4.1. Mode Hierarchy

The modes' complex eigenvalues, shown in Figure 1c, all have magnitudes just below unity, indicating a quasi-steady state. Oscillation frequencies (proportional to the eigenvalue's argument) increase with mode number. Because SVD-based DMD orders modes by decreasing amplitude, the lowest-frequency modes here have the largest amplitudes.

The amplitude, c_i, can be physically understood in terms of total energy across the simulation

$$E_i = 2|c_i|^2 \Delta V \tag{8}$$

where ΔV is the cell volume and the factor 2 compensates for discarding negative frequencies. Figure 1d shows energy generally decays with mode number, though not as an exponential or power law. Since the highest modes contribute negligible energy, our chosen rank was sufficient.

DMD is a dimensionality-reduction and feature extraction technique, so we limit the number of modes analyzed. We calculate the modes' cumulative energy, with the fraction of the total shown in Figure 1e. Since DMD modes are non-orthogonal their summed energies are greater than the reconstructed superposition. The first five modes each contribute over 10% and together exceed 75%. We therefore restrict our analysis to these modes.

We also quantify the energy partition (Figure 1f), calculated for each energy type by multiplying the mode energy by the sum of absolute squares across relevant eigenvector components. Kinetic and magnetic energies dominate, with internal energy significantly smaller. Kinetic energy dominates the first three modes, mode 3 has near-equipartition between magnetic and kinetic energies, and magnetic energy dominates from mode 4 onwards. In MHD wave theory the energy partition depends on wave mode, propagation angle, and plasma β, thus these differences likely reflect distinct physical processes and/or regions with varying plasma parameters.

4.2. Mode Structure

Here we examine the spatial structure of an example mode—mode 2 (1.6 mHz). Figures 2a and 2b shows the total energy density in the equatorial (xy) and terminator (yz) planes, respectively. Peaks in energy occur along the equilibrium magnetopause, approximated by the open–closed boundary (OCB) of the time-averaged magnetic field $\mathbf{B}_0$ (dashed line); determined via field-line tracing (Mejnertsen et al., 2021) and $15 \times 15 \times 15$-cell median filtering topologies to remove fine-scale structure. All modes peak around the magnetopause, though (as we shall see later) at differing locations. Mode 2's energy is largest at the equatorial dawn (positive-y) magnetopause from the terminator to several tens of R_E downtail (Figure 2a). A similar but weaker enhancement is present on the dusk (negative-y) flank, likely due to the lower shear. Energy gradually decreases toward higher latitudes (Figure 2b). Tailward-of-the-cusp reconnection produces localized, aperiodic energy enhancements in the northern/southern lobes persistent in all modes. A weaker energy enhancement is seen along the bow shock.

Given our focus on the magnetopause, we transform to boundary-aligned coordinates. For each z-plane OCB contour we compute the tangential distance from the subsolar point and the local normal, defining a region around the magnetopause (dashed-gray in Figure 2a) that we "unwrap" as the normal–tangent plane in Figures 2c–2f, where data has been interpolated. We focus only on the dawn flank; results for dusk were qualitatively similar. Figure 2c clearly demonstrates mode 2's energy localization both to the magnetopause and in local time. The energy rapidly increases at $\sim$40 R_E tangential distance (around the terminator), remains large for $\sim$25 R_E, then

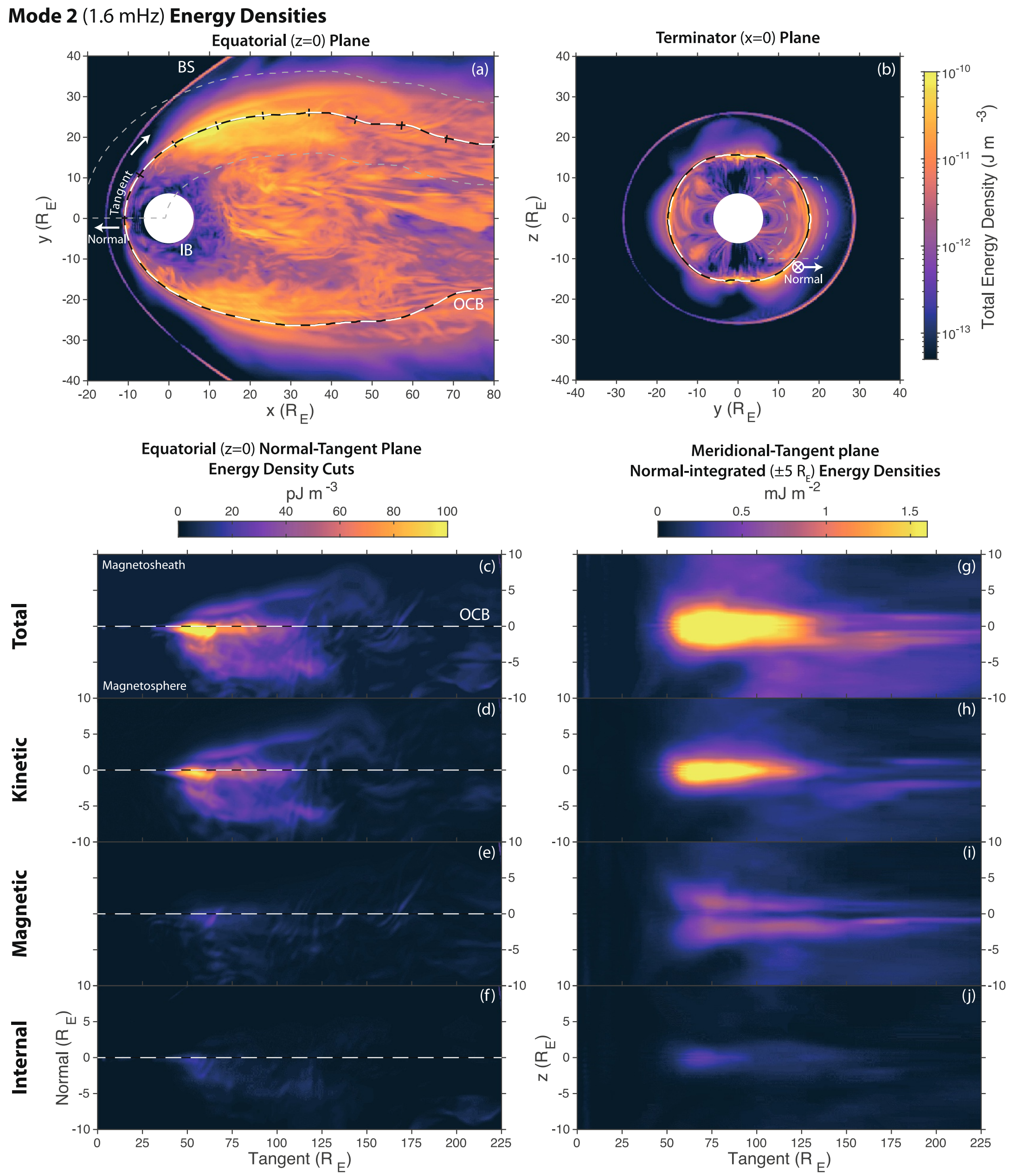

Figure 2. Mode 2 energy densities in (a, b) Gorgon simulation and (c–h) unwrapped magnetopause co-ordinates, where (a, b, c, and g) total, (d, h) kinetic, (e, i) magnetic, and (f, j) internal energy densities are shown. The equilibrium Open–Closed Boundary is displayed (dashed), with markers representing 25 R_E-spacing. Unwrapped magnetopause co-ordinate planes (gray dashed) are also shown.

slowly decays but remains non-negligible for a further ~75 R_E. Normal-extents of energy enhancements increase downtail. Decomposing the total energy density, we find mostly kinetic (Figure 2d) energy in the equatorial plane with only small contributions from magnetic (Figure 2e) and internal (Figure 2f) energies.

Similar qualitative features occur across the other 4 modes—all show (primarily kinetic) energy enhancements around the OCB. Differences arise mainly in where along the magnetopause the energy is significant (discussed later) and, for the nightside magnetopause (tangential distances > 50 R_E), in the precise location along the OCB-normal where the energy peaks. For example, mode 1 peaks slightly earthward of the OCB whereas mode 2's maxima are along it. Boundary layer thickness may be leading to distinct (e.g., inner/outer) modes here (Kivelson & Pu, 1984; Lee et al., 1981), as seen in previous simulations (Claudepierre et al., 2008; Guo et al., 2010; Merkin et al., 2013). However, we stress all modes' enhanced energies overlap, suggesting they are not entirely independent.

Investigating the meridional behavior, for each z-plane we integrate the energy density within ±5 R_E normal distance from the equilibrium OCB (see Figure 2b) and plot the results in the meridional–tangent plane (Figures 2g–2j). Mode 2's energy is mostly constrained within several R_E of the equatorial magnetosphere. This is because the velocity shear becomes more field-aligned out of the equatorial plane, reducing the instability's driver and providing enhanced stabilization (Figure S1 in Supporting Information S1). While kinetic energy still dominates overall (Figure 2h), it is more meridionally confined than the total (Figure 2g) as while magnetic energy (Figure 2i) exhibits a minimum at the equator, it increases with latitude peaking within a few R_E (though smaller in magnitude than the kinetic energy peak). This is expected for wave displacements with even north–south symmetry, where magnetic field vectors have a node at the equator (Singer & Kivelson, 1979). Internal energy (Figure 2j) follows a similar pattern to kinetic, although remains weak. The energy's meridional extent tends to shrink downtail as magnetospheric field lines become more tangentially elongated (Milan et al., 2017), increasing the stabilizing component (Figure S1 in Supporting Information S1). The other modes show similar equatorial localization.

Thus far only mode magnitudes have been used. However, as complex numbers they also contain phase information. While vector component phases depend on the relevant local coordinate system, the (linear) total pressure fluctuation, $\delta p_{\mathrm{tot}} = \delta p + \mathbf{B}_0 \cdot \delta\mathbf{B}/\mu_0$, is a coordinate-independent scalar that should remain continuous across the magnetopause (Walker, 1981). We reconstruct δp_{tot} for each mode (inverting Equations 4–6). Mode 2's real part across the equatorial plane shown in Figure 3a. Well-defined wavelike behavior occurs along the magnetopause flanks with wavefronts approximately normal to the OCB; also true for other modes. The waves extend further into the magnetosheath than the magnetosphere, even perturbing the bow shock analogously to dayside surface eigenmodes (Archer et al., 2021).

We transform δp_{tot} into the normal–tangent plane (Figure 3b), omitting the meridional–tangent plane where large-scale wavefronts are simply oriented vertically. The wavelength varies along the magnetopause, with the tangential distance between peaks/troughs becoming longer downtail. We attempt to quantify this through the phase of δp_{tot}, shown in Figure 3c, calculating the local wave vector $\mathbf{k}$ as its negative gradient (after unwrapping in each dimension to render it continuous). Although finite differencing results are noisy, trends become clearer after appropriate smoothing. A 6.25 × 1 R_E moving average is used in Figure 3d, motivated by the scales of linear surface waves (Archer et al., 2024). Mode 2's local wavelength is shortest on the dayside becoming longer with tangential distance, with a slight decrease in the far tail. This is more obviously seen in Figure 3e, where the ±1 R_E normally averaged local wavelength is plotted (gray) along with polynomial fit (black dashed). Near the subsolar point mode 2's wavelength was below 10 R_E, lengthening to ∼35 R_E at ∼110 R_E tangential distance before temporarily shortening in the far tail.

This wavelength trend approximately follows the background plasma velocity along the OCB, shown in red, a rough proxy for the expected vortex speed. A similar trend is reflected in the other flank. The Pearson correlation coefficient between comparable polynomial fits was 0.946. The velocity does not simply increase monotonically, as often assumed (Haaland et al., 2019). Deceleration within the boundary layer may reflect KH-related plasma transport, where non-linear rolled-up vortices in the far tail thicken the boundary layer slowing plasma within it (Hasegawa et al., 2004; Merkin et al., 2013).

4.3. Superposition of Modes

Having presented the structure of mode 2 in detail, we now compare energies and wavelengths for all 5 modes. Figure 4a shows the energy density along the equatorial magnetopause integrated within ±5 R_E normally of the OCB and ±6.5 R_E in z. Mode 2 is clearly the most significant overall, growing in energy from ∼30 R_E tangential distance to a peak at ∼70 R_E. Linear stability analysis (Miura & Pritchett, 1982) reveals this is where its frequency is most-unstable (Figure S2 in Supporting Information S1). While theory suggests mode 2 should also be highly unstable at ∼4 R_E, large tangential-derivatives in conditions at the dayside magnetopause may create competition amongst modes closely spaced in frequency. Following its peak, mode 2 slowly decays via some dissipation mechanism likely related to wave nonlinearity, though its energy still remains significant throughout.

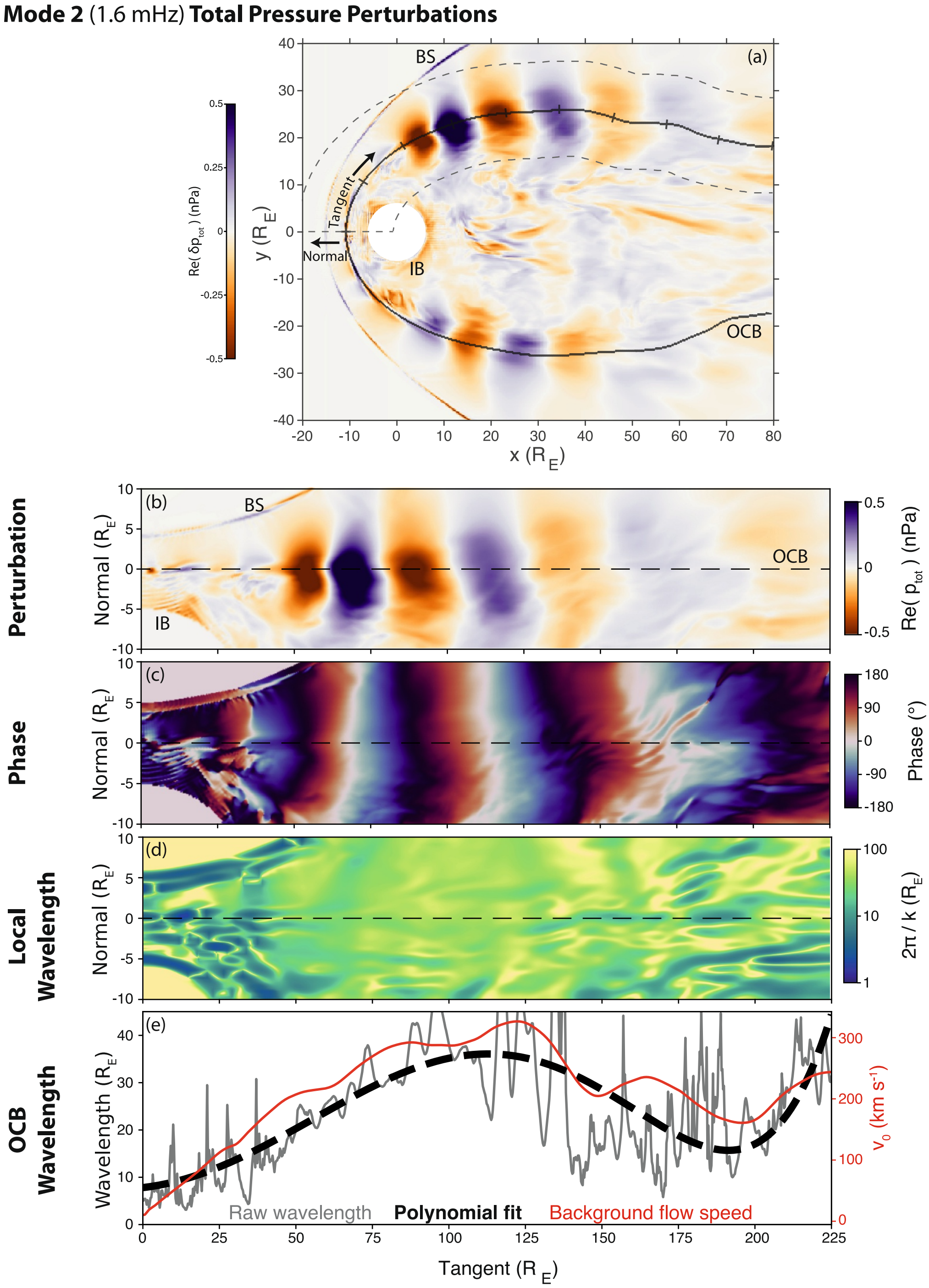

Figure 3. Mode 2 total pressure perturbations in a similar format to Figure 2. Displayed are the real part of the (a, c) reconstructed perturbations, (b, d) phase, (e) local wavelength (2-dimensional 6.25 × 1 R_E smoothing of wave vectors reduces visual noise), and (f) wavelength at the Open–Closed Boundary with 6th-order polynomial fit (dashed) and background flow speed (red).

Mode 1 (1.1 mHz) initially demonstrates similar growth/decay, becoming locally dominant nearer the subsolar point (at ∼15 R_E), again in agreement with linear theory (Figure S2 in Supporting Information S1). It grows before mode 2 is theoretically most-unstable, likely quenching other modes' growth until farther downtail where conditions vary more gradually. From ∼35 R_E mode 1's energy starts slowly increasing again, reaching a larger

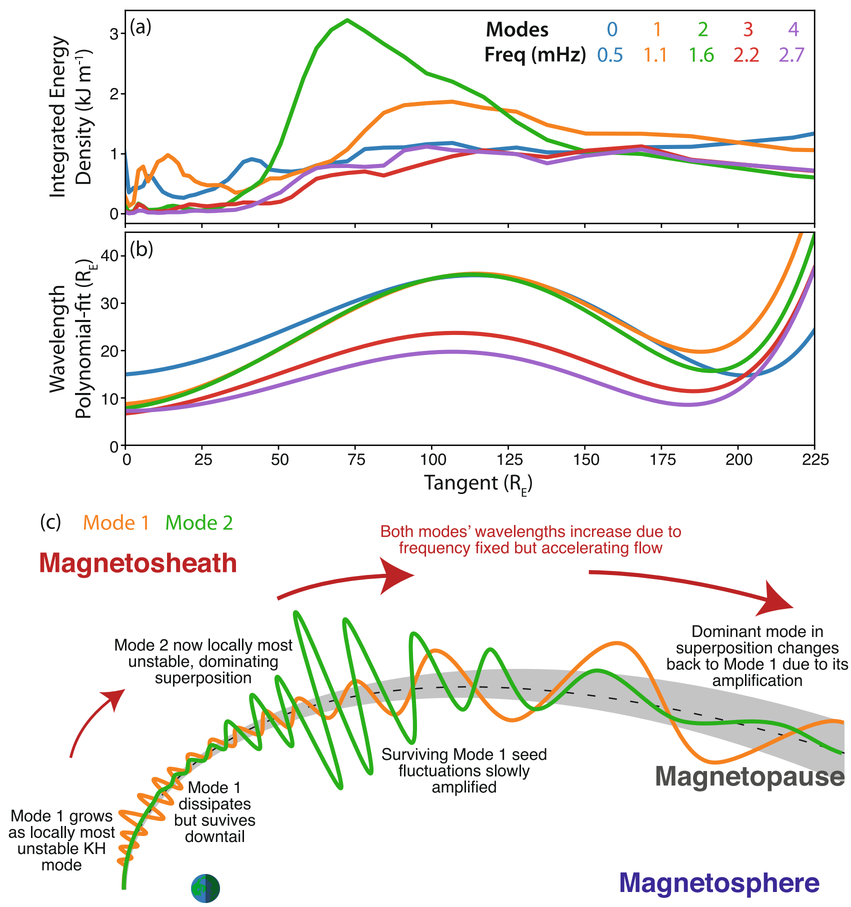

Figure 4. Comparison of dynamic mode decomposition modes along equatorial magnetopause tangent showing (a) integrated energy densities and (b) polynomial-fit wavelengths. (c) Cartoon depicting key results.

peak at $\sim 100\ R_E$ with comparable energy to mode 2 (in its decay phase). This second growth phase coincides with mode 2's initial one but is much more gradual, since it was slightly off the instability maximum. While mode 1 subsequently slowly dissipates, it still becomes the dominant mode again by $\sim 125\ R_E$ because mode 2 decays faster.

Mode 0 (0.5 mHz) curiously has an initial peak at the subsolar point, ranging $\sim 10\ R_E$ tangential distance ($\sim$2 h of local time). Given the weak velocity shear, this cannot be KH-related. Instead, a magnetopause surface eigenmode (Chen & Hasegawa, 1974; Hartinger et al., 2015) may be resonantly excited out of the boundary perturbations—the frequency is certainly within the expected range (Archer & Plaschke, 2015; Plaschke et al., 2009). While mode 0 decays outside the region where MSE can azimuthally stand (Archer et al., 2021), it starts growing again briefly becoming dominant at $\sim 40\ R_E$. Following this, the mode grows gradually eventually becoming dominant for a second time near the end of the simulation domain. Linear theory predicts mode 0, while KH-unstable throughout, never corresponds to the most-unstable mode across the flank (Figure S2 in Supporting Information S1).

Modes 3–4 never become dominant. Their energies only gradually increase along the magnetopause with no significant peaks. This behavior does not resemble a clear instability, though they were certainly related to the magnetopause. Figure S2 in Supporting Information S1 suggests they are surface waves which never correspond to the locally most-unstable KH-mode, but which the KHI is still able to amplify (Nakamura et al., 2020; Nykyri et al., 2017).

Figure 4b compares polynomial fits of the local wavelength along the OCB, derived the same way as in Figure 3e. Although finite-differencing noise of $\sim \pm 10\ R_E$ limits quantitative accuracy, clear qualitative patterns of

10.1029/2025GL120284

wavelength evolution emerge. All modes show similar lengthening from the subsolar point to the flank, with temporary shortening in the far tail. Surprisingly, modes 1–2 have similar wavelengths throughout despite 45% different frequencies, diverging only near the end of the simulation. Mode 0 also has comparable wavelengths between ~75–175 R_E, despite its much lower frequency. Thus, these three modes must have significantly different phase speeds, perhaps due to their different locations within the boundary layer (Kivelson & Pu, 1984). Mode 0, however, has a longer wavelength around the subsolar point, synonymous with surface eigenmodes (Archer et al., 2021). Modes 3–4 have shorter wavelengths with phase speeds broadly consistent with mode 2.

5. Discussion

This work demonstrates a superposition of discrete KH-modes exists at every point along the magnetopause. Modes 1–2 demonstrate clear growth phases, quickly becoming locally dominant mode before slowly decaying with their energies never becoming negligible, as illustrated in Figure 4c. This is consistent with the simulation of Merkin et al. (2013), who showed while KH-growth occurs quickly the subsequent decay is slow (particularly in the outer layer), leading to a spectrum of oscillations. Each modes' growth phase broadly coincides with where its wavelength matches the fastest-growing linear KH-mode, as also verified in other global simulations (Guo et al., 2010; Merkin et al., 2013; Michael et al., 2021).

An additional point to this KH superposition, however, is that fixed-frequency modes can continue to grow in energy much further downtail even when they no longer match the most unstable linear mode, in agreement with Guo et al. (2010) and Archer et al. (2021). Modes 0–1 continue to slowly grow after their initial KH-growth/decay, even across the region mode 2 is clearly most-unstable. Modes 3–4 never demonstrate obvious instability features, never corresponding to the fastest-growing KH-mode, yet still slowly gain energy throughout the simulation. Our global simulation therefore demonstrates that upstream KH-modes can act as seed fluctuations that are re-amplified by the instability much further downtail, altering which mode is locally dominant as illustrated in the cartoon. Consequently, the dominant oscillation at a given point on the magnetopause need not correspond to the locally fastest-growing KH-mode, an assumption often made in interpreting simulations (Guo et al., 2010; Merkin et al., 2013) and observations (Hasegawa et al., 2004; Lin et al., 2014). This potentially explains the KH-wave statistics at lunar distance of Zhou et al. (2022).

The KH-wavelength along the magnetopause varies, with the overall trend for each fixed-frequency mode being a lengthening downtail. Past works (Lin et al., 2014; Merkin et al., 2013) have attributed this solely to boundary layer thickening changing the locally fastest-growing KH-mode (Miura & Pritchett, 1982; Walker, 1981). This, however, is inconsistent with observational statistics in the far tail (Zhou et al., 2022) and cannot account for wavelength changes seen here across growth and decay phases for each fixed-frequency mode. The wavelength variation correlates with the boundary layer flow speed, which approximates the local KH phase velocity (Hasegawa et al., 2009; Palermo et al., 2011), suggesting the flow's acceleration modifies the wavelength. In Earth's inertial frame, a single excited KH-mode's frequency is necessarily fixed everywhere, just like in DMD modes. The accelerating advective magnetosheath flow around the magnetosphere changes the mode's phase velocity, Doppler shifting the wavelength as it travels downtail. Although absolute wavelengths in simulations are resolution-dependent (Text S2 in Supporting Information S1), this relative trend offers a physical explanation for the observed systematically longer-than-expected tail wavelengths (Zhou et al., 2022). Crucially, DMD's ability to isolate phase patterns of distinct fixed-frequency modes (Figure 4c) has revealed this effect. The wavelength's Doppler extension also increases the mode's region of influence normal to the boundary (Archer et al., 2024), as seen in Figures 2a and 2c, so initially mesoscale KH-modes become more globally significant as they propagate. The wavelength variation in our simulation is considerable, up to ~30% proportional change over a single cycle. This not only introduces fundamental differences between temporal (e.g., as necessitated by spacecraft observations, Hasegawa et al., 2004; Rice et al., 2022) and spatial (as more readily employed in simulation snapshots, Guo et al., 2010; Li et al., 2012) wavelength definitions; but questions basic KH-theory, which has little considered tangential plasma inhomogeneity (Fujita et al., 1996; Miura & Pritchett, 1982; Turkakin et al., 2013; Walker, 1981), warranting further exploration.

Our results also suggest multiple KH frequencies with the same (or similar) wavelengths can coexist within the boundary layer. Modes 0–2 have comparable wavelengths across a wide region of the magnetopause, despite different frequencies and thus phase speeds. While these modes highly overlap, indicative of coupled behavior, their local peak energies occur at slightly different normal depths within the boundary layer. This behavior matches linear theory for a suitably thin finite shear layer (Kivelson & Pu, 1984). However, global simulations comparing wave properties and coupling between co-existing KH-modes in the boundary layer (Claudepierre et al., 2008; Guo et al., 2010; Li et al., 2013; Li et al., 2012; Merkin et al., 2013) remain inconsistent and need further reconciliation.

Finally, we have pioneered DMD-usage within space-physics simulations, focusing specifically on KH-dynamics. However, this method could be easily applied to MHD, particle-in-cell (Lapenta, 2012), or Vlasov (Palmroth et al., 2018) simulations of other waves, instabilities and turbulence across the heliosphere (Bruno & Carbone, 2013; Tsurutani et al., 2023). DMD could also prove a powerful tool in analyzing and forecasting oscillations (such as ULF waves) when applied to vast networks of observations, like radars (Fenrich et al., 2021) and ground magnetometers (Xie et al., 2023a, 2023b); and remote-sensing, for instance, auroral, and soft X-ray imaging on the upcoming SMILE mission (Wang et al., 2025).

Conflict of Interest

The authors declare no conflicts of interest relevant to this study.

Availability Statement

The data used in this study is available at Zenodo via doi 10.5281/zenodo.17442416 with a Creative Commons Attribution Non-Commercial No Derivatives 4.0 International License (Kelly, 2025).

Acknowledgments
This work used the Imperial College High Performance Computing Service (doi: 10.14469/hpc/2232). HKM was supported by Science and Technology Facilities Council (STFC) studentship ST/W507519/1. MOA was supported by UKRI (STFC/EPSRC) Stephen Hawking Fellowship EP/T01735X/1 and UKRI Future Leaders Fellowship MR/X034704/1. HKM and MOA also acknowledge funding from the International Space Science Institute (ISSI) in Bern, through ISSI International Team Project 546 "Magnetohydrodynamic Surface Waves at Earth's Magnetosphere (and Beyond)." JPE, JWBE, and JPC acknowledge funding by NERC Grant NE/P017142/1. JPE, JWBE, MH, and JPC acknowledge funding by NERC Grant NE/V003070/1. MH was additionally supported by Schmidt Science Fellows, in partnership with the Rhodes Trust.

References

Albidah, A. B., Brevis, W., Fedun, V., Ballai, I., Jess, D. B., Stangalini, M., et al. (2020). Proper orthogonal and dynamic mode decomposition of sunspot data. *Philosophical Transactions of the Royal Society A: Mathematical, Physical and Engineering Sciences*, *379*(2190), 20200181. https://doi.org/10.1098/rsta.2020.0181

Alford-Lago, D. J., Curtis, C. W., Ihler, A. T., & Zawdie, K. A. (2023). Scale-separated dynamic mode decomposition and ionospheric forecasting. *Radio Science*, *58*(8), 1–24. https://doi.org/10.1029/2022RS007637

Archer, M. O., Hartinger, M. D., Plaschke, F., Southwood, D. J., & Rastaetter, L. (2021). Magnetopause ripples going against the flow form azimuthally stationary surface waves. *Nature Communications*, *12*(1), 5697. https://doi.org/10.1038/s41467-021-25923-7

Archer, M. O., Pilipenko, V. A., Li, B., Sorathia, K., Nakariakov, V. M., Elsden, T., & Nykyri, K. (2024). Magnetopause MHD surface wave theory: Progress & challenges. *Frontiers in Astronomy and Space Sciences*, *11*, 1407172. https://doi.org/10.3389/fspas.2024.1407172

Archer, M. O., & Plaschke, F. (2015). What frequencies of standing surface waves can the subsolar magnetopause support? *Journal of Geophysical Research: Space Physics*, *120*(5), 3632–3646. https://doi.org/10.1002/2014JA020545

Axford, W. I., & Hines, C. O. (1961). A unifying theory of high-latitude geophysical phenomena and geomagnetic storms. *Canadian Journal of Physics*, *39*(10), 1433–1464. https://doi.org/10.1139/p61-172

Belmont, G., & Chateur, G. (1989). Advances in magnetopause Kelvin-Helmholtz instability studies. *Physica Scripta*, *40*(1), 124–128. https://doi.org/10.1088/0031-8949/40/1/018

Briard, A., Ripoll, J.-F., Michael, A., Gréa, B.-J., Peyrichon, G., Cosmides, M., et al. (2024). The inviscid incompressible limit of Kelvin–Helmholtz instability for plasmas. *Frontiers in Physics*, *12*, 1383514. https://doi.org/10.3389/fphy.2024.1383514

Bruno, R., & Carbone, V. (2013). The solar wind as a turbulence laboratory. *Living Reviews in Solar Physics*, *20*. https://doi.org/10.12942/lrsp-2013-2

Chandrasekhar, S. (1961). *Hydrodynamic and hydromagnetic stability*. Oxford University Press.

Chen, L., & Hasegawa, A. (1974). A theory of long-period magnetic pulsations: 2. Impulse excitation of surface Eigenmode. *Journal of Geophysical Research*, *79*(7), 1033–1037. https://doi.org/10.1029/JA079i007p01033

Chittenden, J. P., Lebedev, S. V., Jennings, C. A., Bland, S. N., & Ciardi, A. (2004). X-ray generation mechanisms in three-dimensional simulations of wire array Z-pinches. *Plasma Physics and Controlled Fusion*, *46*(12B), B457–B476. https://doi.org/10.1088/0741-3335/46/12B/039

Ciardi, A., Lebedev, S. V., Frank, A., Blackman, E. G., Chittenden, J. P., Jennings, C. J., et al. (2007). The evolution of magnetic tower jets in the laboratory. *Physics of Plasmas*, *14*(5), 056501. https://doi.org/10.1063/1.2436479

Claudepierre, S. G., Elkington, S. R., & Wiltberger, M. (2008). Solar wind driving of magnetospheric ULF waves: Pulsations driven by velocity shear at the magnetopause. *Journal of Geophysical Research*, *113*(A5), A05218. https://doi.org/10.1029/2007JA012890

Collado-Vega, Y. M., Kessel, R. L., Shao, X., & Boller, R. A. (2007). MHD flow visualization of magnetopause boundary region vortices observed during high-speed streams. *Journal of Geophysical Research*, *112*(A6), A06213. https://doi.org/10.1029/2006JA012104

Desai, R. T., Freeman, M. P., Eastwood, J. P., Eggington, J. W. B., Archer, M. O., Shprits, Y. Y., et al. (2021). Interplanetary shock-induced magnetopause motion: Comparison between theory and global magnetohydrodynamic simulations. *Geophysical Research Letters*, *48*(16), e2021GL092554. https://doi.org/10.1029/2021GL092554

Eggington, J. W. B., Coxon, J. C., Shore, R. M., Desai, R. T., Mejnertsen, L., Chittenden, J. P., & Eastwood, J. P. (2022). Response timescales of the magnetotail current sheet during a geomagnetic storm: Global MHD simulations. *Frontiers in Astronomy and Space Sciences*, *9*, 966164. https://doi.org/10.3389/fspas.2022.966164

Eggington, J. W. B., Eastwood, J. P., Mejnertsen, L., Desai, R. T., & Chittenden, J. P. (2020). Dipole tilt effect on magnetopause reconnection and the steady-state magnetosphere-ionosphere system: Global MHD simulations. *Journal of Geophysical Research: Space Physics*, *125*(7), e2019JA027510. https://doi.org/10.1029/2019JA027510

Eggington, J. W. B., Mejnertsen, L., Desai, R. T., Eastwood, J. P., & Chittenden, J. P. (2018). Forging links in Earth's plasma environment. *Astronomy & Geophysics*, *59*, 6–26. https://doi.org/10.1093/astrogeo/aty275

Faganello, M., & Califano, F. (2017). Magnetized Kelvin–Helmholtz instability: Theory and simulations in the Earth's magnetosphere context. *Journal of Plasma Physics*, *83*(6), 535830601. https://doi.org/10.1017/S0022377817000770

Fenrich, F. R., Rankin, R., Sydorenko, D., Archer, W. E., & Knudsen, D. J. (2021). Birkeland current boundary flows associated with field line resonances. *Journal of Geophysical Research: Space Physics*, *126*(3), e2020JA028896. https://doi.org/10.1029/2020JA028896

Fujita, S., Glassmeier, K.-H., & Kamide, K. (1996). MHD waves generated by the Kelvin-Helmholtz instability in a nonuniform magnetosphere. *Journal of Geophysical Research*, *101*(A12), 27317–27325. https://doi.org/10.1029/96JA02676

Grimmich, N., Settino, A., Nykyri, H. K., Archer, M. O., Blasl, K.-A., Pöppelwerth, A., et al. (2025). Comparison of Kelvin–Helmholtz waves observed simultaneously at the dawn and dusk flanks of the Earth's magnetopause. *Planetary and Space Science*, *267*, 106182. https://doi.org/10.1016/j.pss.2025.106182

Guo, X. C., Wang, C., & Hu, Y. Q. (2010). Global MHD simulation of the Kelvin-Helmholtz instability at the magnetopause for northward interplanetary magnetic field. *Journal of Geophysical Research*, *115*(A10), A10218. https://doi.org/10.1029/2009JA015193

Haaland, S., Runov, A., Artemyev, A., & Angelopoulos, V. (2019). Characteristics of the Flank magnetopause: THEMIS observations. *Journal of Geophysical Research: Space Physics*, *124*(5), 3421–3435. https://doi.org/10.1029/2019JA026459

Hartinger, M. D., Plaschke, F., Archer, M. O., Welling, D. T., Moldwin, M. B., & Ridley, A. (2015). The global structure and time evolution of dayside magnetopause surface Eigenmodes. *Geophysical Research Letters*, *42*(8), 2594–2602. https://doi.org/10.1002/2015GL063623

Hasegawa, H., Fujimoto, M., Phan, T.-D., Rème, H., Balogh, A., Dunlop, M. W., et al. (2004). Transport of solar wind into Earth's magnetosphere through rolled-up Kelvin–Helmholtz vortices. *Nature*, *430*(7001), 755–758. https://doi.org/10.1038/nature02799

Hasegawa, H., Retinò, A., Vaivads, A., Khotyaintsev, Y., André, M., Sonnerup, B. U. Ö., et al. (2009). Kelvin-Helmholtz waves at the Earth's magnetopause: Multiscale development and associated reconnection. *Journal of Geophysical Research*, *114*(A12), A12207. https://doi.org/10.1029/2009JA014042

Hastie, T., Tibshirani, R., & Friedman, J. H. (2009). *The elements of statistical learning: Data mining, inference, and prediction*. Springer. https://doi.org/10.1007/978-0-387-84858-7

Johnson, J. R., Wing, S., & Delamere, P. A. (2014). Kelvin-Helmholtz instability in planetary magnetospheres. *Space Science Reviews*, *184*(1–4), 1–31. https://doi.org/10.1007/s11214-014-0085-z

Kavosi, S., & Raeder, J. (2015). Ubiquity of Kelvin–Helmholtz waves at Earth's magnetopause. *Nature Communications*, *6*(1), 7019. https://doi.org/10.1038/ncomms8019

Kavosi, S., Raeder, J., Johnson, J. R., Nykyri, K., & Farrugia, C. J. (2023). Seasonal and diurnal variations of Kelvin-Helmholtz instability at terrestrial magnetopause. *Nature Communications*, *14*(1), 2513. https://doi.org/10.1038/s41467-023-37485-x

Kelly, H. M. (2025). Superposition of doppler-shifting magnetopause1 Kelvin-Helmholtz modes through dynamic mode 2 decomposition of a global MHD simulation [Dataset]. *Zenodo*. https://doi.org/10.5281/ZENODO.17442416

Kivelson, M. G., & Chen, S.-H. (1995). The magnetopause: Surface waves and instabilities and their possible dynamical consequences. In *Physics of the magnetopause* (pp. 257–268). American Geophysical Union (AGU). https://doi.org/10.1029/GM090p0257

Kivelson, M. G., & Pu, Z.-Y. (1984). The Kelvin-Helmholtz instability on the magnetopause. *Planetary and Space Science*, *32*, 1335–1341. https://doi.org/10.1016/0032-0633(84)90077-1

Koopman, B. O. (1931). Hamiltonian systems and transformations in Hilbert space. *Proceedings of the National Academy of Sciences of the United States of America*, *17*(5), 315–318. https://doi.org/10.1073/pnas.17.5.315

Landa, V., & Reuveni, Y. (2023). Assessment of dynamic mode decomposition (DMD) model for ionospheric TEC map predictions. *Remote Sensing*, *15*(2), 365. https://doi.org/10.3390/rs15020365

Lapenta, G. (2012). Particle simulations of space weather. *Journal of Computational Physics*, *231*(3), 795–821. https://doi.org/10.1016/j.jcp.2011.03.035

Lee, L. C., Albano, R. K., & Kan, J. R. (1981). Kelvin-Helmholtz instability in the magnetopause-boundary layer region. *Journal of Geophysical Research*, *86*(A1), 54–58. https://doi.org/10.1029/JA086iA01p00054

Li, W. Y., Wang, C., Tang, B., Guo, X., & Lin, D. (2013). Global features of Kelvin-Helmholtz waves at the magnetopause for northward interplanetary magnetic field. *Journal of Geophysical Research: Space Physics*, *118*(8), 5118–5126. https://doi.org/10.1002/jgra.50498

Li, W. Y., Guo, X. C., & Wang, C. (2012). Spatial distribution of Kelvin-Helmholtz instability at low-latitude boundary layer under different solar wind speed conditions. *Journal of Geophysical Research*, *117*(A8), A08230. https://doi.org/10.1029/2012JA017780

Lin, D., Wang, C., Li, W., Tang, B., Guo, X., & Peng, Z. (2014). Properties of Kelvin-Helmholtz waves at the magnetopause under northward interplanetary magnetic field: Statistical study. *Journal of Geophysical Research: Space Physics*, *119*(9), 7485–7494. https://doi.org/10.1002/2014JA020379

Masson, A., & Nykyri, K. (2018). Kelvin–Helmholtz instability: Lessons learned and ways forward. *Space Science Reviews*, *214*(4), 71. https://doi.org/10.1007/s11214-018-0505-6

Mehta, P. M., Linares, R., & Sutton, E. K. (2018). A quasi-physical dynamic reduced order model for thermospheric mass density via Hermitian space-dynamic mode decomposition. *Space Weather*, *16*(5), 569–588. https://doi.org/10.1029/2018SW001840

Mejnertsen, L., Eastwood, J. P., & Chittenden, J. P. (2021). Control of magnetopause flux rope topology by non-local reconnection. *Frontiers in Astronomy and Space Sciences*, *8*, 758312. https://doi.org/10.3389/fspas.2021.758312

Mejnertsen, L., Eastwood, J. P., Hietala, H., Schwartz, S. J., & Chittenden, J. P. (2018). Global MHD simulations of the Earth's bow shock shape and motion under variable solar wind conditions. *Journal of Geophysical Research: Space Physics*, *123*(1), 259–271. https://doi.org/10.1002/2017JA024690

Merkin, V. G., Lyon, J. G., & Clausepierre, S. G. (2013). Kelvin-Helmholtz instability of the magnetospheric boundary in a three-dimensional global MHD simulation during northward IMF conditions. *Journal of Geophysical Research: Space Physics*, *118*, 5478–5496. https://doi.org/10.1002/jgra.50520

Michael, A. T., Sorathia, K. A., Merkin, V. G., Nykyri, K., Burkholder, B., Ma, X., et al. (2021). Modeling Kelvin-Helmholtz instability at the high-latitude boundary layer in a global magnetosphere simulation. *Geophysical Research Letters*, *48*(19), e2021GL094002. https://doi.org/10.1029/2021GL094002

Milan, S. E., Clausen, L. B. N., Coxon, J. C., Carter, J. A., Walach, M.-T., Laundal, K., et al. (2017). Overview of solar wind–magnetosphere–ionosphere–atmosphere coupling and the generation of magnetospheric currents. *Space Science Reviews*, *206*(1–4), 547–573. https://doi.org/10.1007/s11214-017-0333-0

Mills, K. J., Longbottom, A. W., Wright, A. N., & Ruderman, M. S. (2000). Kelvin-Helmholtz instability on the magnetospheric flanks: An absolute and convective instability approach. *Journal of Geophysical Research*, *105*(A12), 27685–27699. https://doi.org/10.1029/1999JA000289

Miura, A. (1982). Nonlinear evolution of the magnetohydrodynamic Kelvin-Helmholtz instability. *Physical Review Letters*, *49*(11), 779–782. https://doi.org/10.1103/PhysRevLett.49.779

Miura, A., & Pritchett, P. L. (1982). Nonlocal stability analysis of the MHD Kelvin-Helmholtz instability in a compressible plasma. *Journal of Geophysical Research*, *87*(A9), 7431–7444. https://doi.org/10.1029/JA087iA09p07431

Nakamura, T. K. M., Stawarz, J. E., Hasegawa, H., Narita, Y., Franci, L., Wilder, V., et al. (2020). Effects of fluctuating magnetic field on the growth of the Kelvin-Helmholtz instability at the Earth's magnetopause. *Journal of Geophysical Research: Space Physics*, *125*(3), e2019JA027515. https://doi.org/10.1029/2019JA027515

Nykyri, K., Ma, X., Dimmock, A., Foullon, C., Otto, A., & Osmane, A. (2017). Influence of velocity fluctuations on the Kelvin-Helmholtz instability and its associated mass transport. *Journal of Geophysical Research: Space Physics*, *122*(9), 9489–9512. https://doi.org/10.1002/2017JA024374

Palermo, F., Faganello, M., Califano, F., Pegoraro, F., & Le Contel, O. (2011). Compressible Kelvin-Helmholtz instability in supermagnetosonic regimes. *Journal of Geophysical Research*, *116*(A4), A04223. https://doi.org/10.1029/2010JA016400

Palmroth, M., Ganse, U., Pfau-Kempf, Y., Battarbee, M., Turc, L., Brito, T., et al. (2018). Vlasov methods in space physics and astrophysics. *Living Reviews in Computational Astrophysics*, *4*, 1. https://doi.org/10.1007/s41115-018-0003-2

Plaschke, F., Glassmeier, K.-H., Auster, H. U., Constantinescu, O. D., Magnes, W., Angelopoulos, V., et al. (2009). Standing Alfvén waves at the magnetopause. *Geophysical Research Letters*, *36*(2), L02104. https://doi.org/10.1029/2008GL036411

Pu, Z.-Y., & Kivelson, M. G. (1983). Kelvin-Helmholtz instability at the magnetopause: Solution for compressible plasmas. *Journal of Geophysical Research*, *88*(A2), 841–852. https://doi.org/10.1029/JA088iA02p00841

Rice, R. C., Blasl, K. A., Nykyri, K., Kavosi, S., Sorathia, K. A., & Liou, Y.-L. (2024). Multi-scale processes of the Kelvin-Helmholtz instability at Earth's magnetopause. *Frontiers in Astronomy and Space Sciences*, *11*, 1464010. https://doi.org/10.3389/fspas.2024.1464010

Rice, R. C., Nykyri, K., Ma, X., & Burkholder, B. L. (2022). Characteristics of Kelvin–Helmholtz waves as observed by the MMS from September 2015 to March 2020. *Journal of Geophysical Research: Space Physics*, *127*(3), e2021JA029685. https://doi.org/10.1029/2021JA029685

Rot, M., Horvat, M., & Kosec, G. (2022). Dynamic mode decomposition as an analysis tool for time-dependent partial differential equations. In *International multidisciplinary conference on computer and energy science (SpliTech)*. https://doi.org/10.23919/SpliTech55088.2022.9854243

Schmid, P. J. (2010). Dynamic mode decomposition of numerical and experimental data. *Journal of Fluid Mechanics*, *656*, 5–28. https://doi.org/10.1017/S0022112010001217

Schmid, P. J. (2022). Dynamic mode decomposition and its variants. *Annual Review of Fluid Mechanics*, *54*(1), 225–254. https://doi.org/10.1146/annurev-fluid-030121-015835

Sen, A. K. (1963). Stability of hydromagnetic Kelvin-Helmholtz discontinuity. *Physics of Fluids*, *6*(8), 1154–1163. https://doi.org/10.1063/1.1706875

Singer, H. J., & Kivelson, M. G. (1979). The latitudinal structure of Pc 5 waves in space: Magnetic and electric field observations. *Journal of Geophysical Research*, *84*(A12), 7213–7222. https://doi.org/10.1029/JA084iA12p07213

Slinker, S. P., Fedder, J. A., Sibeck, D. G., Lyon, J. G., Frank, L. A., & Mukai, T. (2003). Simulation of magnetopause oscillations observed January 9, 1996. *Geophysical Research Letters*, *30*(11), 1569. https://doi.org/10.1029/2003GL017063

Southwood, D. J. (1968). The hydromagnetic stability of the magnetospheric boundary. *Planetary and Space Science*, *16*(5), 587–605. https://doi.org/10.1016/0032-0633(68)90100-1

Tanaka, T. (1994). Finite volume TVD scheme on an unstructured grid system for three-dimensional MHD simulation of inhomogeneous systems including strong background potential fields. *Journal of Computational Physics*, *111*(2), 381–389. https://doi.org/10.1006/jcph.1994.1071

Trattner, K. J., Petrinec, S. M., & Fuselier, S. A. (2021). The location of magnetic reconnection at Earth's magnetopause. *Space Science Reviews*, *217*(3), 41. https://doi.org/10.1007/s11214-021-00817-8

Tsurutani, B. T., Zank, G. P., Sterken, V. J., Shibata, K., Nagai, T., Mannucci, A. J., et al. (2023). Space plasma physics: A review. *IEEE Transactions on Plasma Science*, *51*(7), 1595–1655. https://doi.org/10.1109/TPS.2022.3208906

Turkakin, H., Rankin, R., & Mann, I. R. (2013). Primary and secondary compressible Kelvin-Helmholtz surface wave instabilities on the Earth's magnetopause. *Journal of Geophysical Research: Space Physics*, *118*(7), 4161–4175. https://doi.org/10.1002/jgra.50394

Walker, A. D. M. (1981). The Kelvin-Helmholtz instability in the low-latitude boundary layer. *Planetary and Space Science*, *29*(10), 1119–1133. https://doi.org/10.1016/0032-0633(81)90011-8

Walker, A. D. M. (2005). *Magnetohydrodynamic waves in geospace*. Institute of Physics Publishing.

Wang, C., Branduardi-Raymont, G., Escoubet, C. P., & Forsyth, C. (2025). Solar wind magnetosphere ionosphere link explorer (SMILE): Science and mission overview. *Space Science Reviews*, *221*(1), 9. https://doi.org/10.1007/s11214-024-01126-6

Wu, C. (1986). Kelvin-Helmholtz instability at the magnetopause boundary. *Journal of Geophysical Research*, *91*(A3), 3042–3060. https://doi.org/10.1029/JA091iA03p03042

Xie, Z.-K., Zong, Q. G., Ren, J., Yue, C., Liu, Z.-Y., Liu, J.-J., et al. (2023a). Global ULF waves excited by solar wind dynamic pressure impulses: 1. Timescales and geomagnetic activity dependence. *Journal of Geophysical Research: Space Physics*, *128*(10), e2023JA031813. https://doi.org/10.1029/2023JA031813

Xie, Z.-K., Zong, Q. G., Ren, J., Yue, C., Liu, Z.-Y., Liu, J.-J., et al. (2023b). Global ULF waves excited by solar wind dynamic pressure impulses: 2. The spatial distribution asymmetry. *Journal of Geophysical Research: Space Physics*, *128*(10), e2023JA031826. https://doi.org/10.1029/2023JA031826

Yee, K. S. (1966). Numerical solution of initial boundary value problems involving Maxwell's equations in isotropic media. *IEEE Transactions on Antennas and Propagation*, *14*(3), 302–307. https://doi.org/10.1109/tap.1966.1138693

Zhou, Y., Shue, J.-H., Hasegawa, H., Lu, J., Wang, M., & Zhang, H. (2022). Spatial scales of the velocity shear layer and Kelvin-Helmholtz waves on the magnetopause: First statistical results. *Geophysical Research Letters*, *49*(4), e2021GL097271. https://doi.org/10.1029/2021GL097271

References From the Supporting Information

Beit-Sadi, M., Krol, K., & Wynn, A. (2021). Data-driven feature identification and sparse representation of turbulent flows. *International Journal of Heat and Fluid Flow*, *88*, 108766. https://doi.org/10.1016/j.ijheatfluidflow.2020.108766

Bjerhammar, A. (1951). Application of calculus of matrices to method of least squares: With special reference to geodetic calculations. *Elander*.

Bohon, M. D., Orchini, A., Bluemner, R., Paschereit, C. O., & Gutmark, E. J. (2021). Dynamic mode decomposition analysis of rotating detonation waves. *Shock Waves*, *31*(7), 637–649. https://doi.org/10.1007/s00193-020-00975-8

Burtsev, A., He, W., Zhang, K., Theofilis, V., Taira, K., & Amitay, M. (2022). Linear modal instabilities around post-stall swept finite wings at low Reynolds numbers. *Journal of Fluid Dynamics*, *944*, A6. https://doi.org/10.1017/jfm.2022.420

Chatterjee, A. (2000). An introduction to the proper orthogonal decomposition. *Current Science*, *78*, 808–817.

Hyvärinen, A. (1984). Independent component analysis: Recent advances. *Philosophical transactions. Series A, Mathematical, physical, and engineering sciences*, *371*, 20110534. https://doi.org/10.1098/rsta.2011.0534

Moore, E. H. (1920). The fourteenth western meeting of the American mathematical society. *Bulletin of the American Mathematical Society*, *26*, 385–396.

Neumann, J. V. (1932). Proof of the quasi-ergodic hypothesis. *Proceedings of the National Academy of Sciences of the United States of America*, *18*(1), 70–82. https://doi.org/10.1073/pnas.18.1.70

Penrose, R. (1955). A generalized inverse for matrices. *Mathematical Proceedings of the Cambridge Philosophical Society*, *51*(3), 406–413. https://doi.org/10.1017/S0305004100030401

Sorathia, K. A., Merkin, V. G., Ukhorskiy, A. Y., Mauk, B. H., & Sibeck, D. G. (2017). Energetic particle loss through the magnetopause: A combined global MHD and test-particle study. *Journal of Geophysical Research: Space Physics*, *133*(9), 9329–9343. https://doi.org/10.1002/2017JA024268

Trefethen, L. N., & Bau, D. (1997). *Numerical linear algebra*. Society for Industrial and Applied Mathematics.

Tu, J. H., Rowley, C. W., Luchtenburg, D. M., Brunton, S. L., & Kutz, J. N. (2014). On dynamic mode decomposition: Theory and applications. *Journal of Computational Dynamics*, *1*(2), 391–421. https://doi.org/10.3934/jcd.2014.1.391